# Journal Pre-proof

The role of IRT in the archaeometric study of ancient glass through XRF and FORS.

Francesca Micheletti ,   Jacopo Orsilli ,   Jacopo Melada ,
Marco Gargano ,   Nicola Ludwig ,   Letizia Bonizzoni

Please cite this article as:  Francesca Micheletti ,   Jacopo Orsilli ,   Jacopo Melada ,   Marco Gargano ,   Nicola Ludwig ,   Letizia Bonizzoni , The role of IRT in the archaeometric study of ancient glass through XRF and FORS., *Microchemical Journal* (2019), doi: https://doi.org/10.1016/j.microc.2019.104388

This is a PDF file of an article that has undergone enhancements after acceptance, such as the addition of a cover page and metadata, and formatting for readability, but it is not yet the definitive version of record. This version will undergo additional copyediting, typesetting and review before it is published in its final form, but we are providing this version to give early visibility of the article. Please note that, during the production process, errors may be discovered which could affect the content, and all legal disclaimers that apply to the journal pertain.

**Highlights**

- Flux, chromophores and opacifiers determined by XRF and FORS.

- Hypothesis of the use of local sand from XRF data

- FORS suitable for chromophores identification also on transparent materials

- Conservation state and degraded mapped through PT and processed by high order statistical analysis.

- PT output: single image for simple, fast and effective degraded glass mapping.

# The role of IRT in the archaeometric study of ancient glass through XRF and FORS.

Francesca Micheletti[a], Jacopo Orsilli[a], Jacopo Melada[a], Marco Gargano[a], Nicola Ludwig[a], Letizia Bonizzoni[a]

*[a] Dipartimento di Fisica, Università degli Studi di Milano, via Celoria 16, 20133 Milano (Italy)*

Corresponding author: Letizia Bonizzoni, Dipartimento di Fisica, Università degli Studi di Milano, via Celoria 16, 20161 Milano (Italy).
letizia.bonizzoni@mi.infn.it

## Abstract

The process of degradation of archaeological glass subjected to centuries of burial can be of great relevance: typical consequence of degradation in the original vitreous material is rainbow-like iridescence due to chemical alteration of surface layers, salts formation and ion migration. The research presented in this paper is focused on the study of a collection of Roman glass (I - II century A.D.) held by the Museo Civico Etnografico Archeologico Fanchini of Oleggio, Italy. Chemical characterization (namely flux, chromophores and opacifiers determination) has been performed by a combination of X-Ray Fluorescence (XRF) and Fibre Optics Reflectance Spectroscopy (FORS) in the UV-Vis-NIR region. Conservation conditions have been studied and degraded areas have been mapped through Infrared thermography (IRT). IRT is a non-invasive method typically used to measure the apparent temperature of objects and represent it as pseudo-colour images. In the present work, we demonstrate the feasibility of IRT for identifying and mapping glass substrate defects due to ageing of glass, assuming that they may be considered as thermal anomalies. Thermogram sequences have been processed by high order statistical analysis, which is particularly suitable since it is based on automated processes where the output is a single representative image. The use of a thermal camera allows furthermore to perform remote analysis in areas hardly reachable in a fast and effective way.

**Keywords** in situ non-invasive analyses, Roman glass, impulse-thermography, XRF, FORS, glass degradation.

## 1 Introduction

Old glass is an unstable material even in the best environmental conditions. The main degradation process is the leaching out of alkali ions from the glass network; thus, weathering is strictly linked to the presence of Na and/or K contained in the glass matrix, and their relative amount. Archaeological glass objects found in dry soils are better preserved than those found in moist soils, as water is the main cause of weathering of glass. Moreover, ground and water pH is an important factor for the degradation process of buried glass [1]. Molecular water penetrate into the glass, promoting an ion exchange process between protons from the environment and the glass network. This may cause a local pH increasing, causing further damage as hydroxyl ions attack the silica network [2]. Essentially, alkali moving from the 3D silicon-oxygen network are replaced by hydrogen ions from the water and migrates towards the surface. The formation of distinct leached layers one over the other results in a final crust with thickness varying from 1μm to 25μm; these thin layers are irregular, slightly separated and can peel or flake [3]. They produce optical interference resulting in iridescent colours typical of ancient glass. These high hygroscopic layers can cause condensation processes and glass with high K content are severely damaged by potassium carbonate; for this reason, soda glass is chemically more

stable than potash glass. In general, according to the degradation level, weathered glass can have several visual effects, beyond iridescence: dulling, opaque weathering, a total loss of glassy nature, pitting, cracking of the surface, and discoloration [4].

Degradation effects on ancient glass are mostly studied through destructive methods, such as Scanning Electron Microscope (SEM) [5,6], Secondary-ion Mass Spectrometry (SIMS) [7], Laser Induced Breakdown Spectroscopy (LIBS) [8]. Analyses not requiring any sampling can also be performed, i.e. Optical Microscopy, X-Ray Fluorescence (XRF) [9], Proton Induced X-Ray Emission (PIXE) [10], Raman spectroscopy and Fourier Transformed Infrared Spectroscopy (FTIR) [11]. A few thermographic studies devoted to historical glass are also present in literature [12–15].

The aim of this work is to infer glass composition and to study the degradation process occurring in ancient roman glass without any sampling. We applied XRF (X-Ray Fluorescence) and FORS (Fibre Optics Reflectance Spectroscopy) as they have already demonstrated their synergy on glass composition characterization due to their complementarity [16]. Exploiting active thermography, we propose an innovative methodology to quickly and easily map the areas subjected to degradation: a compete and rapid mapping method is surely of interest for conservation issues and the choice of further local deeper investigation. We thus propose a tool to map the degradation pattern of archaeological glass in an automatic and simple way.

## 2 Materials and Methods
### 2.1 The objects under investigation
The studied artefacts were found in the necropolis of Oleggio, now a small town in northern Italy (Piedmont region), in a Roman sepulchral area archaeologically dated between the Augustan Age and the end of the second century A.D. Later on, Oleggio was excluded from the most important trade routes and this explains the lack of artefacts from the II century A.D. onward. The Celtic and Roman necropolis and its artefacts testify the presence of Vertamocori, a Celtic population, and the following Romanization of the region.

The analysed samples, detailed in table 1, include 10 bottles, 3 bowls, 5 rods, 1 cup, and 1 fragment from a plate. Bottles are of different shapes, all common to other coeval sites in northern Italy. The piriform bottles (bottle with a pear-shaped body, sample 54460 and 54461) were used as *unguentarium* and show a more accurate manufacturing, while the *balsamarium* with a spheroidal body (samples 76395 and 3540 is peculiar of a rather poor production, showing bubbles and more thick walls. The asymmetry of the neck and the body, the irregularities of the lip cut, and the irregular thickness of the walls are all signs of the existence of a local centre of production. The scalloped bowls, sometimes decorated with white opaque fluting (samples 327, 3329 and 3465), are frequently found in both the Aquileia region and the Piedmontese-Ticino influence area and were probably produced in either region. Another frequent type of artefacts found in the Ticino area is the rod (sample 3557, 3656, 3659, 43655 and 66257), whose function is still unknown [17,18]. The only chronologically different object is the opaque blue bead, dating the beginning of fourth century A.D. Some of the samples, namely 1462, 3567, 3681, 54460, 54461, 54994 and 76395, show evident alteration crusts.

### 2.2 Degradation analysis
The main objective of this part of the research is to map the degradation pattern of the archaeological glass in the most straightforward, automatic and simple way. Infrared Thermography (IRT) is a deep-rooted investigation tool in conservation and diagnosis of cultural heritage due to its non-invasiveness [19–21]. It allows to measure the apparent temperature of objects and to represent it as pseudo-colour

images. Nonetheless, to the authors knowledge only few papers report application on glass materials exploiting active thermography [12].

### 2.2.1 Thermography

The thermographic inspection can be carried out following two approaches: active thermography and passive thermography [22,23]. Passive thermography measures the surface apparent temperature of an object without any external heat stimulation at the time of data acquisition. Active thermography involves the generation of thermal differences in the material using an external stimulus. There are various methods of investigation in active thermography, among which the most used are Pulsed Thermography (PT) and Lock-in Thermography (LT) [24]. In PT, the object is heated up for a relatively short time using heat sources e.g. flash lamps. The thermal anomalies appear in response to the application of the thermal excitation pulse. In this work, we assume the flakes on the surface of the glass as thermal anomalies. The investigation procedure in PT can be divided into three phases: 1) thermal excitation, 2) thermograms acquisition at different times, 3) thermograms sequence processing. The PT based on high order statistics is particularly suitable for this purpose since the process of defect detection is automated and the output is a single image [25]. The thermograms sequence for each sample has been acquired using an Avio R500EX-Pro (8-14μm) with 30Hz frame rate in reflectance mode i.e. the thermographic camera and the heat sources are placed on the same side with respect to the sample. The thermal pulse is provided by two Godox WITSTRO AD360 flash lights (360W) which are positioned at 15cm from the inspected object. Thermograms sequences are then processed by high order statistical analysis according to the methodology described in literature [26,27]. Indeed, the temperature evolution after the excitation thermal pulse can be regarded as a statistical distribution that counts how many times a given pixel assumes a specific temperature during the acquisition time. The third (skewness) and fourth (kurtosis) standardized central moment were used to obtain the map of the degraded portions of the glass.

### 2.3 Composition analysis

To get information about sample composition, we applied energy dispersive X-Ray fluorescence (XRF) and Fibre Optics Reflectance Spectroscopy (FORS). Namely, XRF allowed to investigate the elemental composition and to recognise the nature of flux and of chromophores, while FORS gave further information about the chromophores' elements and their chemical state.

### 2.3.1 XRF

XRF analysis has been performed in Energy Dispersive mode, exploiting a Mo anode X-ray tube (25 kV, 0.250 mA and 300 s) and an SDD detector (XGL-SPCM-8100 by XG Lab) with 12.5μm Be window and $30mm^2$ x 450μm Si crystal. The distance between X-Ray tube and samples, and between samples and detector, were respectively 85mm and 20mm. XRF analysis has been performed on all glass samples, allowing the identification of element with Z higher than 14; even though light elements cannot be detected, XRF was chosen since non-destructive techniques were mandatory working on well preserved objects. Moreover, glass constituents (i.e. flux and chromophores) can be recognized on the bases of the detected elements [28]. When performing XRF measurements, the most altered portions, as identified by IRT, has been avoided for the characterization of the bulk.

### 2.3.2 FORS

The detection of the absorption bands has been performed in transmission mode with a Xenon lamp XBO 75W and a Prime X Si-TE thermally cooled spectrometer (B&WT TEK Inc.), working on a

spectral range between 200 and 1000nm with a resolution of 1nm (integration time: 50ms). The radiation was sent and collected with two optical fibres bundles with a total diameter of 5mm each. To avoid overexposure of the detector, a diaphragm has been used to limit the intensity of the light source. The objects under investigation have been analysed on different areas so to overcome thickness and geometrical variability. Altered portions, as identified by IRT, has been avoided for the characterization of the bulk.

## 3 Results and discussion

### 3.1 Thermography

PT images were collected for all degraded samples; in the following, only the results obtained from three of them are presented in detail as prime examples. Light blue samples 1462 and 76395 visually present the major degradation processes; for comparison, sample 3359, with no sign of degradation, is also reported. Silicate glass is semi-transparent in the visible and opaque in the medium and far-infrared region; moreover, it may present high reflectance values for incidence angles greater than 45° [12]. In such kind of materials, the heat diffusion, following the application of a thermal pulse, cannot merely modelled according to the 1D solutions of the Fourier equation in solid semi-infinite media [29]. Several authors already considered the problem of semi-transparent materials inspection by optically excited thermography [30,31]. For these reasons, the analyses were conducted without ascribing the sample behaviour to a predefined model, but only processing the data on a statistical basis, namely considering the third (skewness) and fourth (kurtosis) standardized central moment to obtain the map of the degraded portions of the glass (Fig. 1). It is evident that the skewness and kurtosis values of the probability mass function that describes the value of a pixel (i.e. the temperature) temporal evolution depends on the presence of flakes on the surface of the glass samples. This is due to the change in the diffusion flow driven by the materials' thermal properties discontinuities [32]: when the thermal pulse reaches the defect location, some part of the energy is reflected and the remaining is transmitted. Indeed, the skewness and kurtosis values depends by the thermal diffusivity and the depth of the defects [26,27]. The background, a white paper sheets placed behind the samples, and the unaltered portions of the glass respond in a similar way. They present both skewness and kurtosis values near zero, indicating symmetric and platykurtic distribution, respectively. The temperature distributions of defects are positively-skewed and leptokurtic, instead. It worth noting how the areas showing the lower negative skewness values can be identified as altered portions on the opposite side of the samples. The number of frames used for our investigation is significantly lower than literature data; nonetheless, since investigated objects have thin and semi-transparent walls, a lower number of frames was enough in order to obtain good results, saving time and computational cost.

### 3.2 Chemical composition of glass: the vitreous matrix

Roman historical glass are generally not heavily weathered [33] and this is also due to the Na based matrix. Roman glass, in fact, was obtained by fusing silica from the sand and soda, acting as stabilizer. On the bases of the provenance of the sand used, alumina and lime were present in different amount, too [34–37]. To lower the melting point of silica, a natural soda salt (natron, mainly from dry lake beds in Egypt) was added, acting as flux [38,39]; presence of around 1% to 2% chlorine can be found in Roman glass [37,40]. Elements detected by XRF are Si, P, S, Cl, K, Ca, Ti, Cr, Mn, Fe, Co, Cu, Zn, Sr, Sb, and Pb; position of Compton scattering peak allowed to verify the constancy of geometrical conditions. Semi-quantitative data have been obtained normalizing net peak areas to Mo anode scattering, to account geometry variations, and correcting on the instrumental sensibility, excitation

efficiency and absorption coefficient for each element. Even though they are not concentration values, they can give useful hints about glass composition, mostly when working on close Z element ratios and on the bases of multivariate analyses, in which signals variation is considered, and not the absolute concentration value [41]. As known, XRF spectrometers have a low sensitivity for light elements that are moreover affected by the surface alteration of samples [16]. For this reason, vitreous matrix has been classified mainly on the bases of K, Ca, Mn, Ti and Fe comparison. Namely, the Ca to K ratio permits to infer the nature of the flux [42,43]; in general, the use of ratios allows reducing the effect of systematic errors due to low sensitivity, mostly when characteristic energies considered are comparable. Starting from the consideration that Ca/K concentration ratio higher than 14 should be typical of natron use, while a ratio lower than about 1.5 should indicates the use of plant ashes, we can confirm the soda nature of the samples in study, coherently with the historical period, being the corrected average ratio 17.5 (see tab 2). As detailed later in section 3.2, also the position of Co absorption bands indicates the presence of soda matrix. Before XRF and FORS analyses, IRT has been performed, allowing to map degraded areas; for some samples, however, almost all the surface was affected by alteration. In these cases, is thus possible that altered areas were analysed, especially with XRF, having a larger spot on the sample with respect to FORS. Leach layers, usually about 20 to 100μm, can absorb emission of light elements, unbalancing calculated ratios, namely Ca/K. This could be the case of the rods (samples 3557, 3659 and 43655) for which K peaks are smaller than for all other samples. It is also possible, as discussed later, that these samples, typologically linked to a local production, were made with different raw materials. Besides, when an internal or external source of manganese is present, inclusions of manganese itself can be formed in the leached layer; due to the large spot of the XRF spectrometer, we got an average answer, not sensible to this process [2].

Evaluating both Fe vs Ti and Fe vs Mn ratio (fig. 2), we can make some comments about sand. Mn was often added to the batch because is acts as iron oxidizer and lowers the saturation of colours [44]. In our samples, the good correlation between Fe and Mn (see fig. 2), independently from the colour, seems to indicate no Mn addition. The change from green to amber colour should be linked to Fe and his redox states (ferrous/ferric) also in absence of Mn action, due to uncontrolled melting conditions [45]. In fact, without a careful control of temperature and oxygen partial pressure of the atmosphere and batch, equilibrium between $Fe^{2+}$ and $Fe^{3+}$ can vary also in presence of similar Fe concentration. A lower Mn to Fe ratio is evident for samples 3179, 54994, 54461, three dark blue transparent bottles showing the higher Co content (see table 2). Mn/Fe value reflects in this case the higher amount of Fe due to the addition of Co mineral and it is coherent with the hypothesis of no Mn addiction as low iron sands were selected with the intent of producing colourless or better manufacturing glass [46]. Nonetheless, yellow and amber samples have a lower Mn/Fe ratio (see tab.2). On this same subject, Ti vs Fe bi-plot (fig.2) shows a different correlation for all dark blue samples (including the three dark blue transparent bottles quoted above) and for the transparent and yellow samples, for which Fe oxidation state plays a fundamental role. As both Fe and Ti are considered impurities of the sand, the ratio could indicate two different sources of raw material [47]: indeed, the use of sands from Ticino River for local production of Roman natron-based glass has been considered yet [36]. In our particular case, more complete elemental analyses would be needed to possibly confirm – or deny – this hypothesis. Anyway, the higher presence of Co can again be responsible for the higher amount of Fe of blue samples. Moreover, Co results correlated with Cu presence, as evident in the third graph of fig. 2, for all blue samples; note that Co presence was above instrumental detection limits only for all the blue samples and one among the light blue ones (3824).

Vitreous matrix can be considered together with chromophores contents considering all the element detected in Hierachical Cluster Analyses (Ward linkage, Euclidean distance, standardization of variables) reported in fig. 3. Two main groups can be seen (A and B), with several subgroups and two

outliers, namely the blue opaque bead and sample 3179. The former shows the presence of Sb (opacifier, see section 3.2), and very high Pb signal; lead-glasses has a lower softening temperature and are less affected by the stress which may be caused in the cooling process, so they were preferred to produce small objects as beads [45,48]. The latter has instead an anomalous Fe content. Group B can be divided into two subgroups, C (light blue/transparent objects) and D (dark blue samples, presence of Co). Group A comprehends subgroup E (the rods, with the green one standing out for Cu content, see table 2) characterized by higher Ca/K ratio (Tab. 2) and subgroup F, the bowls and the amber bottle (samples 3465, 3677, 3329) and a light blue fragment (sample 3540, with very low Ca). Blue sample 327 is still a bowl and differentiate due to the presence of Sb from white opaque decorations. This classification gather in group A types of objects frequently found in the Ticino River influence area, suggesting a local production [36] on the base of typological and archaeological considerations. Blue samples 3557 and 327, typologically characteristics of Ticino area, are more similar to other colour samples in Ti vs Fe plot (fig. 2), too.

*3.3 Chemical composition of glass: chromophores and opacifier determination*
Colours in roman glass were linked to the presence of different metallic oxides, both from the raw (such as Fe) and intentionally added (Co or Cu) materials. Firing and cooling conditions can affect the formation of the different oxides. Besides, calcium antimonate was added as opacifier in the Roman period until the II cent. A.D.; XRF data highlight the presence of Sb in the white opaque decorations investigated and in the blue opaque bead.

The determination of chromophores has been performed mainly by FORS, depending the colour on the oxidation state of some metallic elements and not on their concentration alone. Previous works have proved this technique to give interesting results on vitreous materials, allowing a huge amount of information not only about chromophores, but also glassy matrix constituent. In fact, the position of some absorption bands in FORS spectra depends on the vitreous matrix nature [16,23,25,35–37,42].

In the following, the presence of the different oxides is distinguished on the bases of FORS spectra; the spectra in the following figures report the relative transmittance, i.e. the relative transmission of the radiation that crosses the sample, standardized so that all spectra range from 0 to 1.

We should also stress that literature data referring to chromophore band position is quite ambiguous and the same band can be associated to different chromophores or chromophore complexes (Table 3); for instance, 380 nm absorption band can be associated to either $Fe^{3+}$, $Mn^{2+}$ or to a Fe–Mn complex. The deepest reason is that not only the chromophore itself influences the colour, but also all the possible complexes, oxides and molecules that it can create inside the matrix. In this work, we associate every band to the corresponding chromophore or complex taking advantage of the XRF data, and we classify the samples taking into account the major differences in the chromophore influences.

*3.3.1 Colour produced by iron species*
All the samples, regardless of the colour, show the band of $Fe^{3+}$ in the octahedral configuration (280-340nm). In the amber and yellow samples, iron is also associated to the absorption at 380-450nm due to the tetrahedral configuration of $Fe^{3+}$: in this particular configuration, iron presents three absorption bands in this region. If their intensity is high, they result in a unique broad band (fig. 4).

$Fe^{3+}$ is acknowledged for the yellow colour, while $Fe^{2+}$ oxide, with its typical broad band that start to increase at about 950nm, is responsible for the light blue shades. This band is present in all the samples excluded the amber coloured (see fig. 4).

Thus, without the presence of other chromophore, the different shades of colour are linked to the $Fe^{2+}/Fe^{3+}$ ratio, changing from light-blue to amber when the $Fe^{2+}$ relative concentration decreases

[42,47,49]. It is worth to note that yellow and amber samples do not present a higher Fe content in XRF spectra.

In principles, the ratio of the two iron oxidation states can give information about production technology. [50] In the present case, the very different thickness of glass walls together with the consequent variable geometrical measuring conditions, prevented to apply this method as bands intensities were not normalizable.

### 3.3.2 Colour produced by iron species in presence of manganese species

The weak absorption band around 420nm present in light blue/transparent sample FORS spectra (see fig. 4) seems to be due to the iron-manganese complex, depending on the concentration of both iron and manganese as well as of the glass making temperature [51]. Whenever both iron and manganese are present, equilibrium exists between the blue ferric ion, the yellow ferrous ion, the red ion $Mn^{3+}$ and the colourless ion $Mn^{2+}$: in reducing melting conditions, the manganese acts as an oxidising agent with respect to iron and a colourless glass is obtained. Absorption bands pattern between 380 and 510nm is very complex, as both $Fe^{3+}$ and the Fe-Mn complex present bands in this region; unlike amber/yellow samples (380-450nm broad band), the iron bands for light blue/transparent samples are deconvoluted.

### 3.3.3 Colour produced by cobalt species

The presence of $Co^{2+}$, responsible for the colour of the dark blue samples, is confirmed by the presence of three overlapping bands at 540, 590 e 640 nm (fig. 4). The spectral position of the cobalt absorption bands shift of about 15nm in presence of a high potassium matrix (due to the use of plant ash as flux) [35], so the shape of the FORS spectra confirms the soda matrix of samples. Co has been found in all the blue samples (327, 3179, 3357, 3359, 54460, 54461, 54494) by XRF (table 2), and as a trace in the light blue sample 3824; in this sample, Co amount is very low and the absorption band of the chromophore are not visible in the FORS spectra, not affecting the colour of the glass. For all blue samples, Co and Cu contents are correlated, and an extra copper content with respect to the iron content is detected compared to the light blue samples (see tab.2), In these cases, instead of the classical green hue (see next section), the small amount of copper oxide may enhance the blue colour, absorbing part of the red radiation.

### 3.3.4 Colour produced by copper species

Copper in glass matrix can be present in two different forms: metallic copper ($Cu^{0}$) which gives a red colour, and its oxide form ($Cu^{2+}$), which gives a bright green colour. In general, the absorption band of $Cu^{2+}$ (775-835nm) can be concealed in our spectra by the high emission peaks of the xenon lamp and by the broad band due to $Fe^{2+}$. The only bright green sample (3656, a rod) has high presence of copper (see tab.2); its FORS spectrum, reported in fig. 4, does not show the transmission band between 340 and 380 nm (resent in yellow samples) and has a broad band between 200 and 450 nm. This behaviour is similar to that of Egyptian green, whose colour is due to the $Cu^{2+}$ ion in an amorphous silica-rich matrix, showing an absorption band between 250 and 350 nm [52]. Sample 3656 spectrum has instead a larger band due to the concomitant presence of $Fe^{3+}$. Even though the spectra of samples 3656 (green), 3659 and 43655 (yellow) are similar, the high content of copper in the green sample shifts the maximum of transmission toward the blue region (from 395nm in 3659 and 43655 samples to 365nm in the green sample), resulting in a bright green colour.

## 4. Conclusions

Twenty-two archaeological Roman (I - II century A.D.) glass from the Museo Civico Etnografico Archeologico Fanchini of Oleggio, Italy, have been analysed to determine the glass matrix elemental composition and identify the element oxides responsible for the colour by means of exclusively non-invasive spectroscopic techniques. In particular, FORS proved to be suitable for chromophores identification. Flux, opacifiers and colouring metal oxides identified are typical of Roman age, even if the use of local sand have been inferred from XRF results.

Furthermore, conservation state and degraded areas have been mapped through remote sensing by PT: processing the data on a statistical basis, we have highlighted the distribution of degraded areas identified as thermal anomalies. Thermogram sequences have been processed by high order statistical analysis, which is particularly suitable for serial analyses since it an automated process and its output is a single image. This also allows an easy interpretation to conservators or non-expert users. On these bases, we demonstrate the potentiality of pulsed thermography as an operational methodology to map in a simple, fast and effective way the presence of flakes in archaeological glass.

**Declaration of interests**

The authors declare that they have no known competing financial interests or personal relationships that could have appeared to influence the work reported in this paper.

9

**References**

[1]   C.M. Jackson, D. Greenfield, L.A. Howie, An Assessment of Compositional and Morphological Changes in Model Archaeological Glasses in an Acid Burial Matrix, Archaeometry. 54 (2012) 489–507. https://doi.org/10.1111/j.1475-4754.2011.00632.x.

[2]   G. Nuyts, S. Cagno, S. Bugani, K. Janssens, Micro-XANES study on Mn browning: use of quantitative valence state maps, J. Anal. At. Spectrom. 30 (2015) 642–650. https://doi.org/10.1039/C4JA00386A.

[3]   H. Römich, E. Lopez, Research on corrosion phenomena of archaeological glass, First International Conference Hyalos - Vitrum - Glass: History, Technology and Conservation of Glass and Vitreous Materials in the Hellenistic World. (2002) 241–247.

[4]   R.G. Newton, S. Davison, Conservation of glass, Butterworth & Co. (Publishers) Ltd., 1989.

[5]   E. Greiner-Wronowa, D. Zabiegaj, P. Piccardo, Glass–metal objects from archaeological excavation: corrosion study, Appl. Phys. A. 113 (2013) 999–1008. https://doi.org/10.1007/s00339-013-7728-x.

[6]   M.-T. Doménech-Carbó, A. Doménech-Carbó, L. Osete-Cortina, M.-C. Saurí-Peris, A Study on Corrosion Processes of Archaeological Glass from the Valencian Region (Spain) and its Consolidation Treatment, Microchim Acta. 154 (2006) 123–142. https://doi.org/10.1007/s00604-005-0472-y.

[7]   S. Fearn, D.S. McPhail, V. Oakley, Room temperature corrosion of museum glass: an investigation using low-energy SIMS, Applied Surface Science. 231–232 (2004) 510–514. https://doi.org/10.1016/j.apsusc.2004.03.205.

[8]   N. Carmona, M. Oujja, E. Rebollar, H. Römich, M. Castillejo, Analysis of corroded glasses by laser induced breakdown spectroscopy, Spectrochimica Acta Part B: Atomic Spectroscopy. 60 (2005) 1155–1162. https://doi.org/10.1016/j.sab.2005.05.016.

[9]   D.J. Huisman, S. Pols, I. Joosten, B.J.H. van Os, A. Smit, Degradation processes in colourless Roman glass: cases from the Bocholtz burial, Journal of Archaeological Science. 35 (2008) 398–411. https://doi.org/10.1016/j.jas.2007.04.008.

[10] A. Climent-Font, A. Muñoz-Martin, M.D. Ynsa, A. Zucchiatti, Quantification of sodium in ancient Roman glasses with ion beam analysis, Nuclear Instruments and Methods in Physics Research Section B: Beam Interactions with Materials and Atoms. 266 (2008) 640–648. https://doi.org/10.1016/j.nimb.2007.12.088.

[11] A. Tournié, P. Ricciardi, Ph. Colomban, Glass corrosion mechanisms: A multiscale analysis, Solid State Ionics. 179 (2008) 2142–2154. https://doi.org/10.1016/j.ssi.2008.07.019.

[12] T. Palomar, F. Agua, M. Gómez- Heras, Comparative assessment of stained-glass windows materials by infrared thermography, International Journal of Applied Glass Science. 9 (2018) 530–539. https://doi.org/10.1111/ijag.12352.

[13] T. Palomar, C. Machado, F. Agua, M. Gómez- Heras, Thermographic analysis of glasses, enamels and grisailles from stained glass windows, in: Proceedings of the 5th GLASSAC International Conference, NOVA.FCT Editorial, Caparica, Portugal, 2017: pp. 94–97.

[14] C. Machado, A. Machado, T. Palomar, L.C. Alves, M. Vilarigues, Debitus grisailles for stained-glass conservation: an analytical study, Cons. Património. (2019). https://doi.org/10.14568/cp2018067.

[15] T. Palomar, M. Silva, M. Vilarigues, I. Pombo Cardoso, D. Giovannacci, Impact of solar radiation and environmental temperature on Art Nouveau glass windows, Heritage Science. 7 (2019) 82. https://doi.org/10.1186/s40494-019-0325-3.

[16] P. Fermo, M. Andreoli, L. Bonizzoni, M. Fantauzzi, G. Giubertoni, N. Ludwig, A. Rossi, Characterisation of Roman and Byzantine glasses from the surroundings of Thugga (Tunisia):

Raw materials and colours, Microchemical Journal. 129 (2016) 5–15. https://doi.org/10.1016/j.microc.2016.05.014.

[17] G. Spagnolo Garzoli, ed., Conubia gentium: la necropoli di Oleggio e la romanizzazione dei Vertamocori : Oleggio, Palazzo Bellini, 23 gennaio-30 aprile 1999, Omega, 1999.

[18] R. Carazzetti, S. Biaggio-Simona, Vetri romani del Cantone Ticino : guida alla mostra, [Locarno]: Museo civico e archeologico, c1988., n.d. http://lib.ugent.be/catalog/rug01:001659668.

[19] J. Melada, M. Gargano, I. Veronese, N. Ludwig, Does electro-osmosis work in moisture damage prevention? Applicability of infrared-based methods to verify water distribution under electric fields, Journal of Cultural Heritage. 31 (2018) S38–S45. https://doi.org/10.1016/j.culher.2018.04.009.

[20] K. Mouhoubi, J.L. Bodnar, J.M. Vallet, V. Detalle, Follow-up of restoration of works of art of the patrimony by infrared thermography, in: Optics for Arts, Architecture, and Archaeology VII, International Society for Optics and Photonics, 2019: p. 110581E. https://doi.org/10.1117/12.2525692.

[21] Y. Yao, S. Sfarra, S. Lagüela, C. Ibarra-Castanedo, J.-Y. Wu, X.P.V. Maldague, D. Ambrosini, Active thermography testing and data analysis for the state of conservation of panel paintings, International Journal of Thermal Sciences. 126 (2018) 143–151. https://doi.org/10.1016/j.ijthermalsci.2017.12.036.

[22] C. Ibarra-Castanedo, D. González, M. Klein, M. Pilla, S. Vallerand, X. Maldague, Infrared image processing and data analysis, Infrared Physics & Technology. 46 (2004) 75–83. https://doi.org/10.1016/j.infrared.2004.03.011.

[23] E. D'Accardi, D. Palumbo, R. Tamborrino, U. Galietti, Quantitative analysis of thermographic data through different algorithms, Procedia Structural Integrity. 8 (2018) 354–367. https://doi.org/10.1016/j.prostr.2017.12.036.

[24] G. Giorleo, C. Meola, Comparison between pulsed and modulated thermography in glass–epoxy laminates, NDT & E International. 35 (2002) 287–292. https://doi.org/10.1016/S0963-8695(01)00062-7.

[25] F.J. Madruga, C. Ibarra-Castanedo, O.M. Conde, J.M. López-Higuera, X. Maldague, Infrared thermography processing based on higher-order statistics, NDT & E International. 43 (2010) 661–666. https://doi.org/10.1016/j.ndteint.2010.07.002.

[26] F.J. Madruga, C. Ibarra-Castanedo, O.M. Conde, J.M. Lopez-Higuera, X. Maldague, Automatic data processing based on the skewness statistic parameter for subsurface defect detection by active infrared thermography, in: Proceedings of the 2008 International Conference on Quantitative InfraRed Thermography, QIRT Council, 2008. https://doi.org/10.21611/qirt.2008.12_16_16.

[27] F.J. Madruga, C. Ibarra-Castanedo, O.M. Conde, X.P. Maldague, J.M. López-Higuera, Enhanced contrast detection of subsurface defects by pulsed infrared thermography based on the fourth order statistic moment, kurtosis, in: Thermosense XXXI, International Society for Optics and Photonics, 2009: p. 72990U. https://doi.org/10.1117/12.818684.

[28] L. Bonizzoni, A. Galli, M. Milazzo, Analyses of the stained glasses of Certosa di Pavia, X-Ray Spectrometry. 31 (2002) 35–38. https://doi.org/10.1002/xrs.530.

[29] S.J. Altenburg, H. Weber, R. Krankenhagen, Thickness determination of semitransparent solids using flash thermography and an analytical model, Quantitative InfraRed Thermography Journal. 15 (2018) 95–105. https://doi.org/10.1080/17686733.2017.1331655.

[30] R. Bernegger, S.J. Altenburg, M. Röllig, C. Maierhofer, Applicability of a 1D Analytical Model for Pulse Thermography of Laterally Heterogeneous Semitransparent Materials, International Journal of Thermophysics. 39 (2018) 39. https://doi.org/10.1007/s10765-018-2362-7.

[31] G. Caruso, S. Paoloni, N. Orazi, C. Cicero, U. Zammit, F. Mercuri, Quantitative evaluations by infrared thermography in optically semi-transparent paper-based artefacts, Measurement. 143 (2019) 258–266. https://doi.org/10.1016/j.measurement.2019.04.086.

[32] S. Lugin, Algorithms for efficient and quantitative non-destructive testing by pulsed thermography, in: 2007: p. 14. https://doi.org/10.22028/D291-22414.

[33] R.H. Brill, The record of time in weathered glass, Archaeology. 14 (1961) 18–22.

[34] D. Allen, Roman glass in Britain, Shire Publications, Princes Risborough, Buckinghamshire, 1998.

[35] O. Dussart, B. Velde, P.-M. Blanc, J.-P. Sodini, Glass from Qal'at Sem'an (Northern Syria): The Reworking of Glass during the Transition from Roman to Islamic Compositions, Journal of Glass Studies. 46 (2004) 67–83.

[36] R. Arletti, G. Vezzalini, S. Biaggio Simona, F. Maselli Scotti, Archaeometrical studies of roman imperial age glass from Canton Ticino, Archaeometry. 50 (2008) 606–626. https://doi.org/10.1111/j.1475-4754.2007.00362.x.

[37] T. Palomar, M. Garcia-Heras, R. Sabio, J.-M. Rincon, M.-A. Villegas, Composition, Preservation and Production Technology of Augusta Emerita Roman Glasses from the First to the Sixth Century a.d., Mediterranean Archaeology and Archaeometry. 12 (2012) 193–212.

[38] A. Silvestri, G. Molin, G. Salviulo, R. Schievenin, Sand for Roman Glass Production: An Experimental and Philological Study on Source of Supply*, Archaeometry. 48 (2006) 415–432. https://doi.org/10.1111/j.1475-4754.2006.00264.x.

[39] D. Foy, Composition et propriétés du verre, in: Coeur de verre. Production et diffusion du verre antique - Danièle Foy, Collectif, Infolio, Gollion, 2003: pp. 16–21.

[40] P. Croveri, I. Fragalà, E. Ciliberto, Analysis of glass tesserae from the mosaics of the 'Villa del Casale' near Piazza Armerina (Enna, Italy). Chemical composition, state of preservation and production technology, Appl. Phys. A. 100 (2010) 927–935. https://doi.org/10.1007/s00339-010-5670-8.

[41] L. Bonizzoni, A. Galli, M. Gondola, M. Martini, Comparison between XRF, TXRF, and PXRF analyses for provenance classification of archaeological bricks, X-Ray Spectrometry. 42 (2013) 262–267. https://doi.org/10.1002/xrs.2465.

[42] F. Gallo, A. Silvestri, G. Molin, Glass from the Archaeological Museum of Adria (North-East Italy): new insights into Early Roman production technologies, Journal of Archaeological Science. 40 (2013) 2589–2605. https://doi.org/10.1016/j.jas.2013.01.017.

[43] V. Van der Linden, E. Meesdom, A. Devos, R.V. Dooren, H. Nieuwdorp, E. Janssen, S. Balace, B. Vekemans, L. Vincze, K. Janssens, PXRF, µ-XRF, Vacuum µ-XRF, and EPMA Analysis of Email Champlevé Objects Present in Belgian Museums, Microscopy and Microanalysis. 17 (2011) 674–685. https://doi.org/10.1017/S1431927611011950.

[44] I.C. Freestone, S. Wolf, M. Thirlwall, The production of HIMT glass: elemental and isotopic evidence, in: International Association for the History of Glass (Ed.), Annales Du 16e Congrès de l'Association Internationale Pour l'histoire Du Verre, London, 2003, AIHV, Nottingham, : pp. 153–157.

[45] J. Henderson, S.E. Warren, X-Ray fluorescence analyses of iron age glass: beads from Meare and Glasombury lake villages, Archaeometry. 23 (1981) 83–94. https://doi.org/10.1111/j.1475-4754.1981.tb00958.x.

[46] P. il Vecchio, Storia naturale, Einaudi, Torino, 1997.

[47] E. Gliozzo, A.S. Barbone, F. D'acapito, Waste Glass, Vessels and Window-Panes from Thamusida (morocco): Grouping Natron-Based Blue–Green and Colourless Roman Glasses, Archaeometry. 55 (2013) 609–639. https://doi.org/10.1111/j.1475-4754.2012.00696.x.

[48] W.A. Weyl, The constitution of glasses: a dynamic interpretation. Constitution and properties of some representative glasses., Interscience Publ., 1967.

[49] J.W.H. Schreurs, R.H. Brill, Iron and sulfur related colors in ancient glasses, Archaeometry. 26 (1984) 199–209. https://doi.org/10.1111/j.1475-4754.1984.tb00334.x.

[50] A. Ceglia, W. Meulebroeck, P. Cosyns, K. Nys, H. Terryn, H. Thienpont, Colour and Chemistry of the Glass Finds in the Roman Villa of Treignes, Belgium, Procedia Chemistry. 8 (2013) 55–64. https://doi.org/10.1016/j.proche.2013.03.008.

[51] S.B. Donald, A.M. Swink, H.D. Schreiber, High-iron ferric glass, Journal of Non-Crystalline Solids. 352 (2006) 539–543. https://doi.org/10.1016/j.jnoncrysol.2005.11.042.

[52] S. Pagès- Camagna, S. Colinart, The Egyptian Green Pigment: Its Manufacturing Process and Links to Egyptian Blue*, Archaeometry. 45 (2003) 637–658. https://doi.org/10.1046/j.1475-4754.2003.00134.x.

[53] D. Möncke, M. Papageorgiou, A. Winterstein-Beckmann, N. Zacharias, Roman glasses coloured by dissolved transition metal ions: redox-reactions, optical spectroscopy and ligand field theory, Journal of Archaeological Science. 46 (2014) 23–36. https://doi.org/10.1016/j.jas.2014.03.007.

[54] W. Meulebroeck, K. Baert, H. Wouters, P. Cosyns, A. Ceglia, S. Cagno, K. Janssens, K. Nys, H. Terryn, H. Thienpont, The identification of chromophores in ancient glass by the use of UV-VIS-NIR spectroscopy, in: Optical Sensing and Detection, International Society for Optics and Photonics, 2010: p. 77260D. https://doi.org/10.1117/12.853666.

[55] W. Meulebroeck, H. Wouters, K. Nys, H. Thienpont, Authenticity screening of stained glass windows using optical spectroscopy, Scientific Reports. 6 (2016). https://doi.org/10.1038/srep37726.

[56] P.A. Bingham, C.M. Jackson, Roman blue-green bottle glass: chemical–optical analysis and high temperature viscosity modelling, Journal of Archaeological Science. 35 (2008) 302–309. https://doi.org/10.1016/j.jas.2007.03.011.

[57] L.R. Green, F. Alan Hart, Colour and chemical composition in ancient glass: An examination of some roman and wealden glass by means of ultraviolet-visible-infra-red spectrometry and electron microprobe analysis, Journal of Archaeological Science. 14 (1987) 271–282. https://doi.org/10.1016/0305-4403(87)90015-X.

[58] A. Ceglia, W. Meulebroeck, K. Baert, H. Wouters, K. Nys, H. Thienpont, H. Terryn, Cobalt absorption bands for the differentiation of historical Na and Ca/K rich glass, Surface and Interface Analysis. 44 (2012) 219–226. https://doi.org/10.1002/sia.3810.

[59] P. Mirti, A. Lepora, L. Saguì, Scientific Analysis of Seventh-Century Glass Fragments from the Crypta Balbi in Rome*, Archaeometry. 42 (2000) 359–374. https://doi.org/10.1111/j.1475-4754.2000.tb00887.x.

**Figure captions**
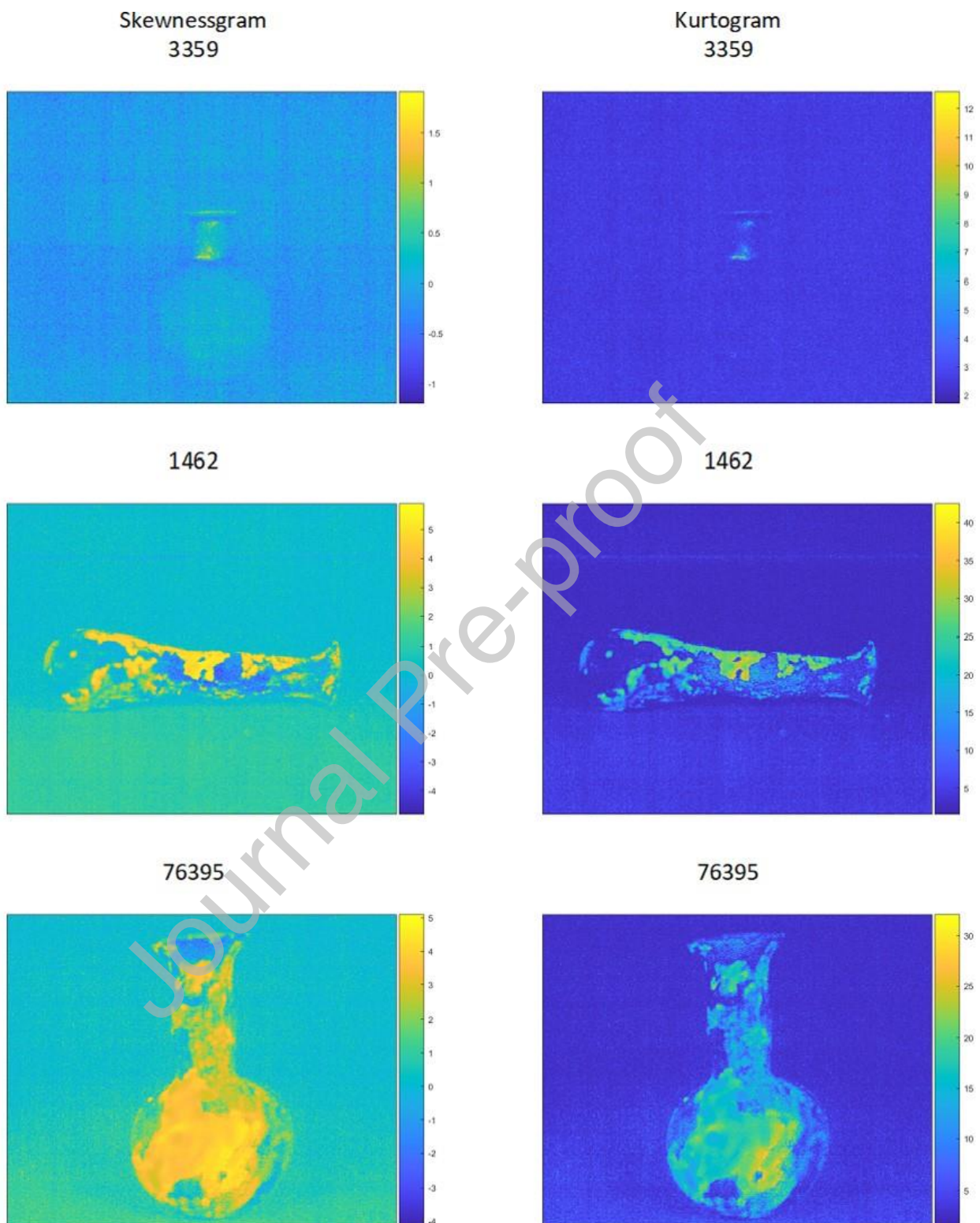
**Fig.1.** Skewness and kurtosis degradation maps for well-preserved sample (3359) and highly degraded samples (1462 and 76395). The surface alteration can be mapped on the basis of the different thermal properties.
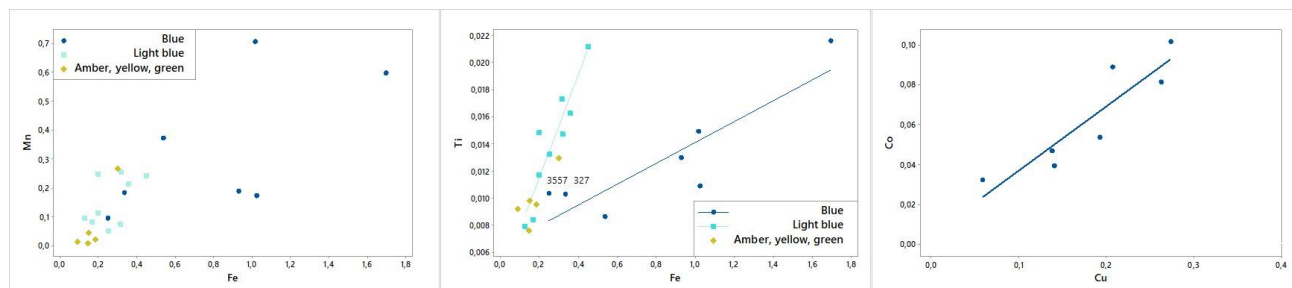
**Fig.2.** Mn vs Fe, Ti vs Fe and Co vs Cu bi-plots for I and II cen. A.D. samples (the blue opaque bead is not reported). Regression lines for Ti/Fe plot have been calculated separately for light blue and blue samples.
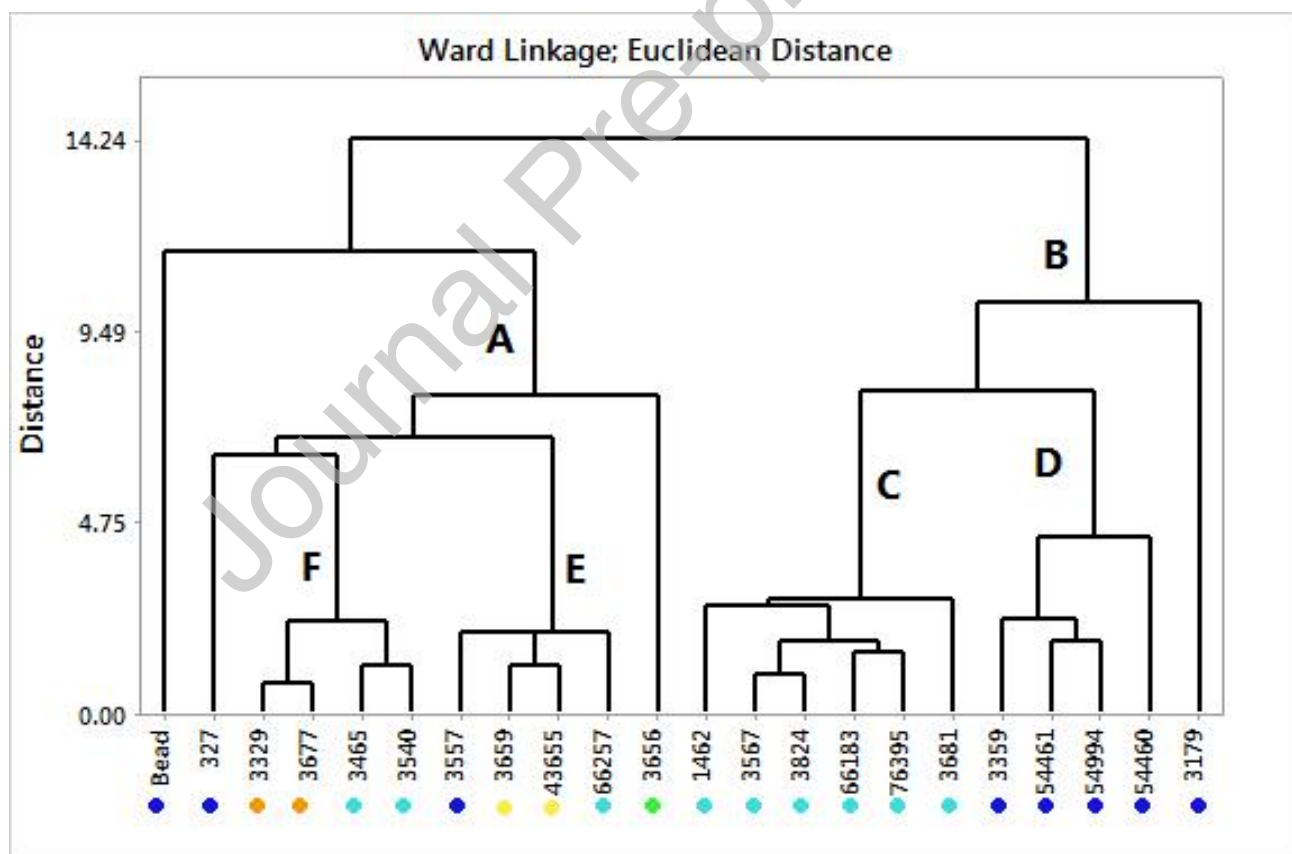


**Fig.3.** Dendrogram obtained considering all the element detected by XRF (Ward linkage, Euclidean distance, standardization of variables). Coloured dots refer to the colour of objects; for group description see end of section 3.1.

16

17
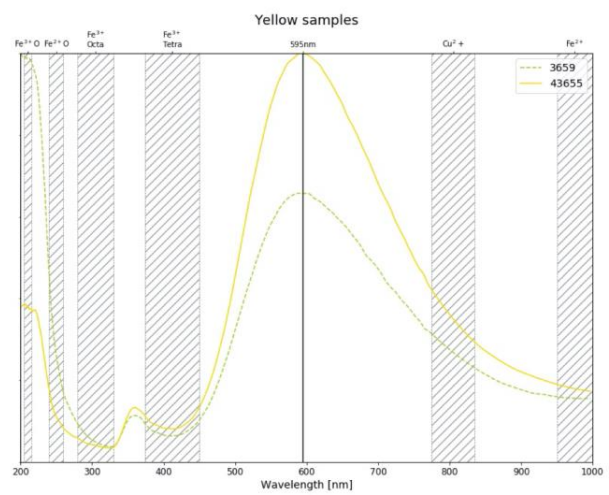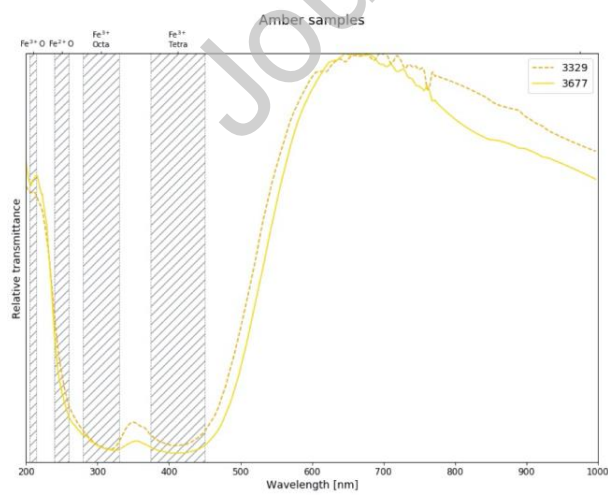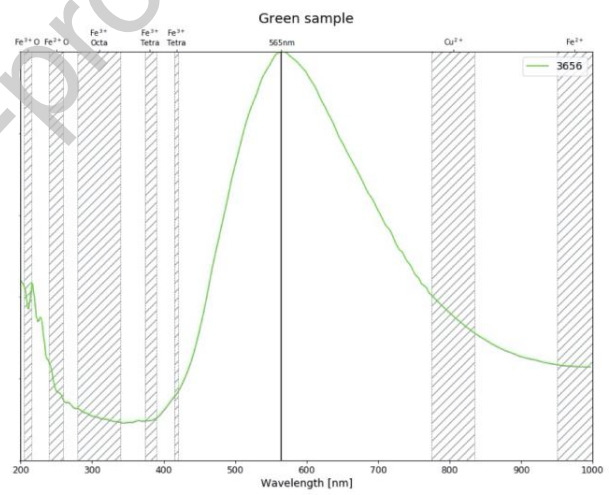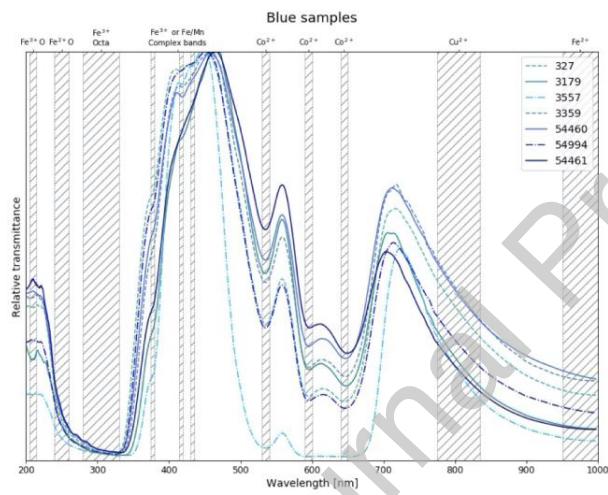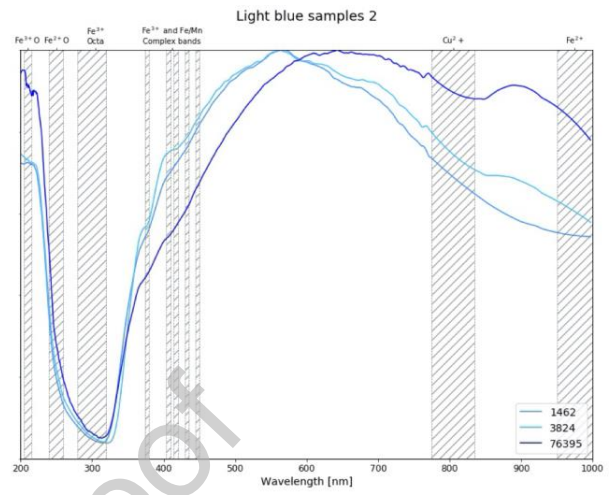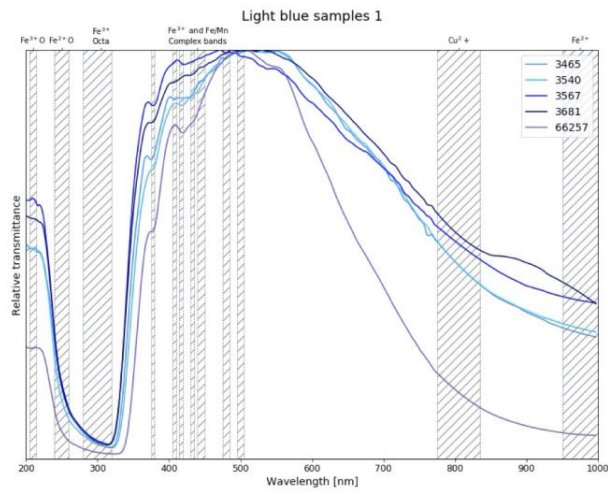
**Fig.4.** FORS spectra of amber and yellow samples (main chromophore: Fe. In the amber samples the main oxidation state is $Fe^{3+}$, in the yellow samples both $Fe^{2+}$ and $Fe^{3+}$ are present.); light blue samples ($Mn^{2+}$ and Fe-Mn complex bands are present in the same region of the tetrahedral $Fe^{3+}$); blue and green samples (all the blue samples have $Co^{2+}$ as main chromophore, while the green sample colour is mainly due to the presence of $Cu^{2+}$, which shifts the transmission maximum). The relative transmission of the radiation that crosses the sample has been standardized so that spectra range from 0 to 1.

**Table 1**: list of the samples with archaeological data

| Sample | Picture | Description | Colour | Period |
|--------|---------|-------------|--------|--------|
| 327 |  | Bowl | Transparent blue with white opaque stripes | I-II cent. AD |
| 1462 |  | Tear-bottle | Light blue, transparent | I cent. AD |
| 3179 |  | Bottle | Blue, transparent | I-II cent. AD |
| 3329 |  | Bowl | Amber with white opaque stripes | I-II cent. AD |
| 3359 |  | Bottle | Blue, transparent | I-II cent. AD |
| 3465 |  | Bowl | Light blue, transparent | I-II cent. AD |
| 3540 |  | Bottle | Light blue, transparent | I-II cent. AD |
| 3557 |  | Rod | Blue and opaque white | I-II cent. AD |
| 3567 |  | Cup | Light blue, transparent | I-II cent. AD |
| 3656 |  | Rod | Green | I-II sec AD |
| 3659 |  | Rod | Yellow and opaque white | I-II cent. AD |
| 3677 |  | Bottle | Amber | I-II cent. AD |
| 3681 |  | Small vial | Light blue, transparent | I-II cent. AD |

| 3824 |  | Bottle with long neck | Light blue, transparent | I-II cent. AD |
|------|------|------|------|------|
| 43655 |  | Rod | Yellow | I-II cent. AD |
| 54460 |  | Bottle with flat bottom | Transparent blue | Beginning of the I cent. AD |
| 54461 |  | Bottle with round bottom | Transparent blue | Beginning of the I cent. AD |
| 54994 |  | Bottle | Transparent blue | Beginning of the I cent. AD |
| 66183 |  | Dish fragment | Light blue, transparent | I-II cent. AD |
| 66257 |  | Rod | Light blue | I-II cent. AD |
| 76395 |  | Bottle | Light blue, transparent | I cent. AD |
| Bead |  | Bead | Blue, opaque | Beginning of the IV cent. AD |

**Table 2**: Ca/K, Mn/Fe, Ti/Fe, Cu/Fe and Co/Fe ratios obtained for glass samples under investigation. For Co, UDL indicates cobalt content under the detection limit of our spectrometer. Ratios are based on net peak areas normalized to Mo anode scattering and corrected on the instrumental sensibility, excitation efficiency and absorption coefficient for each element.

| Sample | Ca/K | Mn/Fe | Ti/Fe | Cu/Fe | Co/Fe |
|---|---|---|---|---|---|
| **Bead** | 15.76 | 0.36 | 0.03 | 1.22 | 0,22 |
| **327** | 16.98 | 0.55 | 0.03 | 0.18 | 0,10 |
| **1462** | 10.05 | 0.54 | 0.05 | 0.32 | UDL |
| **3179** | 8.58 | 0.35 | 0.01 | 0.16 | 0,06 |
| **3329** | 15.93 | 0.10 | 0.05 | 0.06 | UDL |
| **3359** | 8.56 | 0.69 | 0.02 | 0.26 | 0,09 |
| **3465** | 8.57 | 0.74 | 0.06 | 0.17 | UDL |
| **3540** | 9.63 | 0.49 | 0.05 | 0.23 | UDL |
| **3557** | 33.85 | 0.38 | 0.04 | 0.57 | 0,16 |
| **3567** | 12.14 | 0.60 | 0.05 | 0.24 | UDL |
| **3656** | 22.06 | 0.89 | 0.04 | 5.34 | UDL |
| **3659** | 37.22 | 0.28 | 0.07 | 0.16 | UDL |
| **3677** | 11.32 | 0.04 | 0.05 | 0.10 | UDL |
| **3681** | 12.91 | 0.20 | 0.05 | 0.06 | UDL |
| **3824** | 9.43 | 0.80 | 0.05 | 0.22 | 0,02 |
| **43655** | 65.30 | 0.13 | 0.10 | 0.41 | UDL |
| **54460** | 14.48 | 0.70 | 0.01 | 0.26 | 0,08 |
| **54461** | 12.86 | 0.17 | 0.01 | 0.19 | 0,05 |
| **54994** | 12.36 | 0.20 | 0.01 | 0.22 | 0,10 |
| **66183** | 15.67 | 1.25 | 0.08 | 0.09 | UDL |
| **66257** | 16.99 | 0.57 | 0.06 | 0.23 | UDL |
| **76395** | 13.23 | 0.23 | 0.05 | 0.05 | UDL |

**Table 3**: Chromophores and chromophores complexes absorption bands according to literature data.

| Band [nm] | Chromophore | Reference* | Band [nm] | Chromophore | Reference |
|---|---|---|---|---|---|
| 210 | Complex of $Fe^{3+}$-O | [53] | 440 | $Fe^{3+}$ | [54,55] |
| 250 | Complex of $Fe^{2+}$-O | [53] | 445 | $Fe^{3+}$ | [37,56] |
| 258 | $Fe^{3+}$ | [57] | 450 | $Fe^{2+}$ | [54] |
| 279 | $Fe^{3+}$ | [37] | 470-520 | $Mn^{3+}$ | [16,57] |
| 280-340 | $Fe^{3+}$ (Octahedral) | [16] | 480 | Fe-Mn complex | [56] |
| 350-380 | $Fe^{3+}$ | [54] | 480 | $Mn^{3+}$ | [49,53] |
| 352 | $Mn^{2+}$ | [56] | 490 | $Fe^{3+}$ | [57] |
| 375-380 | $Fe^{3+}$ | [16,37,53–57] | 500 | $Mn^{3+}$ | [56] |
| peaks in 375-420 | $Fe^{3+}$ (Tetrahedral) | [58] | 508 | $Mn^{3+}$ | [37] |
| peaks in 375-450 | $Fe^{3+}$ (Tetrahedral) | [58] | 513 | $Mn^{3+}$ | [37] |
| 380 | $Mn^{2+}$ | [56] | 535-540 | $Co^{2+}$ | [16,53–55,57–59] |
| 380 | Fe-Mn complex | [56] | 555 | $Fe^{3+}$ | [53] |
| 400 | $Fe^{2+}$ | [49] | 563 | $Cu^{0}$ | [54] |
| 400-410 | Fe–S complex | [49,53,54] | 595-600 | $Co^{2+}$ | [16,53–55,59] |
| 405 | $Fe^{3+}$ | [57] | 640-650 | $Co^{2+}$ | [16,53–55,59] |
| 415-420 | $Fe^{3+}$ | [16,37,53–57] | 775-780 | $Cu^{2+}$ | [37,54] |
| 420 | Fe–Mn complex | [54–56] | 800 | $Cu^{2+}$ | [53,55] |
| 420 | $Mn^{2+}$ | [53] | 835 | $Cu^{2+}$ | [54,59] |
| 430 | $Mn^{2+}$ | [16] | From 950 | $Fe^{2+}$ | [16] |
| 430 | $Cu^{0}$ | [55] | 1000-1050 | $Fe^{2+}$ | [37,53,55] |
| 430-435 | $Fe^{3+}$ | [37,53,56,57] | 1075-1100 | $Fe^{2+}$ | [49,54,56,57] |
| 440 | Fe–Mn complex | [56] | 1900 | $Fe^{2+}$ | [49] |